Lawrence Berkeley National Laboratory
Laboratory Directorate

Title
A simple algorithm for estimation of source-to-detector distance in Compton imaging

Permalink
https://escholarship.org/uc/item/0t27x93n

Authors
Rawool-Sullivan, Mohini W
Sullivan, John P
Tornga, Shawn R
et al.

A simple algorithm for estimation of source-to-detector distance in Compton imaging

Mohini W. Rawool-Sullivan [a,*], John P. Sullivan [b], Shawn R. Tornga [c], Steven P. Brumby [d]

[a] MS B230, IAT-1, Los Alamos National Laboratory, Los Alamos, NM 87545, USA
[b] MS B244, ISR-1, Los Alamos National Laboratory, Los Alamos, NM 87545, USA
[c] MS D466, ISR-1, Los Alamos National Laboratory, Los Alamos, NM 87545, USA
[d] MS D436, ISR-2, Los Alamos National Laboratory, Los Alamos, NM 87545, USA

ARTICLE INFO

ABSTRACT

Compton imaging is used to predict the location of gamma-emitting radiation sources. The X and Y coordinates of the source can be obtained using a back-projected image and a two-dimensional peak-finding algorithm. The emphasis of this work is to estimate the source-to-detector distance (Z). The algorithm presented uses the solid angle subtended by the reconstructed image at various source-to-detector distances. This algorithm was validated using both measured data from the prototype Compton imager (PCI) constructed at the Los Alamos National Laboratory and simulated data of the same imager. Results show this method can be applied successfully to estimate Z, and it provides a way of determining Z without prior knowledge of the source location. This method is faster than the methods that employ maximum likelihood method because it is based on simple back projections of Compton scatter data.

1. Introduction

Gamma-ray imaging is widely used as a research tool in nuclear medicine and astrophysics. Research in the use of gamma-ray imaging for waste monitoring and nuclear nonproliferation began in the 1990s. The current increased interest in counter terrorism has renewed efforts to develop better gamma-ray detection technologies. Current nuclear search instrumentation for counter terrorism application requires improvements because special nuclear materials (SNM) such as uranium and plutonium are long-lived, and are modest gamma-ray emitters. At the same time, terrestrial gamma-ray backgrounds are large, typically several gamma rays $cm^{-2} s^{-1}$, so detection ranges are currently limited to a few meters. Radiation dispersal devices, wherein conventional explosions may disperse a common radioactive sources such as ^{137}Cs or ^{60}Co, are intrinsically brighter, however, still difficult to detect at a distance. Traditional capabilities consist of detection systems with no inherent directional sensitivity, exacerbating the inherently low signal-to-noise ratio by responding equally to source and off-source background. Pinpointing a nuclear threat is also a difficult task. Only by blinding the instrument to certain directions (collimation) one can obtain a degree of directional selectivity. Such techniques when used from

long distances fail to isolate weak sources against varying terrestrial backgrounds, and even when sources are detected, they cannot be located to the limited area that will allow for interdiction and preventive action. The enhanced sensitivity and wide-field imaging of Compton devices can be exploited to noninvasively monitor or search large areas via ground or airborne platforms. When used at close range, as in surveys of vehicles or containers at fixed checkpoints, the same devices will confidently detect materials of any significant mass and locate them in three dimensions.

In particular, imaging technologies which would allow passive gamma-ray detectors to localize sources and reject backgrounds from irrelevant directions and sources are sought. This capability would provide the improved sensitivity needed for sensing nuclear materials from distances of tens of meters. Compton imaging was recognized as one such imaging technique. This method is based on Compton scattering (scattering of a gamma ray from an electron). Compton scattering preserves information about the direction and energy of incident gamma rays if the scattering byproducts can be precisely measured. Various Compton imaging designs have been studied for use in counterterrorism. One such effort was carried out by the Naval Research Laboratory along with the University of California, Berkeley, and was based on their astrophysics expertise. This effort focused on development of Compton imagers that used thick, position-sensitive, solid-state detectors (Kurfess et al., 2004). Efforts by Lawrence Livermore National Laboratory (along

* Corresponding author. Tel.: +1 505 667 6628; fax: +1 505 665 3456.
E-mail address: Mohini@lanl.gov (M.W. Rawool-Sullivan).
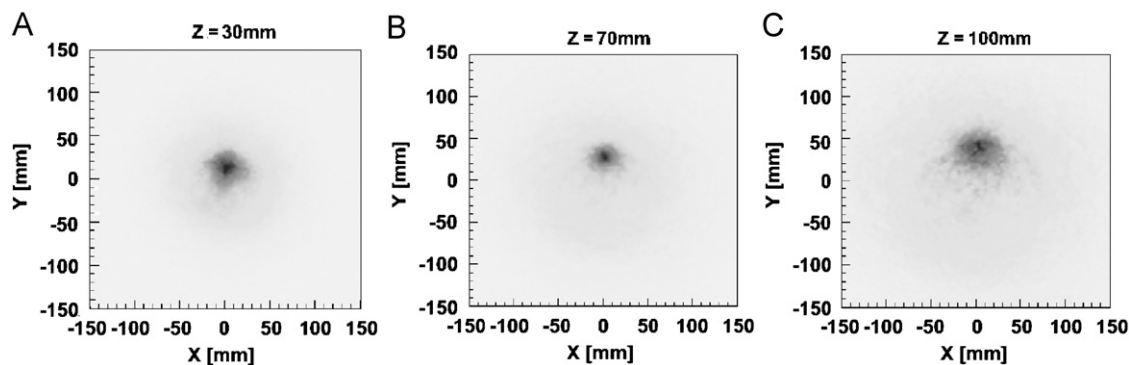
Fig. 1. Reconstructed images using measured data of a ^{137}Cs 'point' source located at $X = 10$ mm, $Y = 38$ mm, and $Z = 70$ mm. The image was reconstructed at various source-to-detector distances, $Z = 30$ mm (A), 70 mm (B), and 100 mm (C).

with collaborators) included the development of a spectroscopic imager for gamma rays (Mihailescu et al., 2007), Compton imaging with position-sensitive silicon and germanium detectors (Vetter et al., 2007), and Compton imaging with coaxial germanium detectors (Niedermayr et al., 2005).

In the works referenced so far, sources are imaged by setting the source-to-detector distance (R) to the known distance. A method for calculating the source-to-detector distance itself was not investigated. In many applications, it is not only necessary to localize a source in a closed volume, with respect to the detector in two dimensions, the source-to-detector distance must also be known. Some attempts at determining the source-to-detector distance using an electronically collimated Compton camera were performed in the fields of medical imaging and waste management applications. Haskins and coworkers studied the point source location accuracy or the error associated with the calculated location of a point source in three dimensions (X, Y, and Z in the Cartesian coordinate system) using both a maximum intensity method and the intensity center-of-gravity method (Haskins et al., 1996). They studied two cases: one in which a waste assay drum was used and another where a small tumor in the human body was explored. For the analysis, they used an adaptation of the maximum likelihood (ML) iterative approach using high-purity germanium (HPGe) detector arrays. Comparisons between the reconstruction of experimental data and simulations showed comparable results. A more recent medical imaging paper by Nguyen et al. (2001) utilizes imaging derived from a linear integral transform directly from a Compton scattering analysis of the image formation.

In this paper, we present an algorithm for estimating the source-to-detector distance for point sources in a Cartesian coordinate system using simple back-projection algorithms. The X and Y coordinates of the source can be obtained using the back-projected image and a two-dimensional peak-finding algorithm (Morhac et al., 1997). The emphasis of the work presented here is to find the source-to-detector distance (Z). The method presented uses the solid angle subtended by the reconstructed images at various source-to-detector distances. This method is much faster than algorithms that use ML methods to estimate the source-to-detector distance. The viability of this algorithm is described using experimental measurements as well as simulated results from the prototype Compton imager (PCI) constructed at Los Alamos National Laboratory (LANL) (Sullivan et al., 2003; Hoover et al., 2006). The basis for this method lies in the fact that reconstructed images using data collected with PCI are of better quality for the 'real' Z distance. This is demonstrated in Fig. 1, which shows reconstructed images for measured data using a single ^{137}Cs source at various source-to-detector distances. The actual source location was (10, 38, 70) mm. For all practical purposes this source

was a point source. The reconstructed image assuming the correct source-to-detector distance, $Z = 70$ mm (Fig. 1B), is better (i.e. the size of the image is smaller) than for other source-to-detector distances, $Z = 30$ and 100 mm (Figs. 1A and C). In addition, when the source is off the central axis of the detector, reconstructing the image at the wrong value of Z also yields incorrect values of X and Y—this can also be seen in Fig. 1. At this time our study is limited to a single point-like source. It is clear that this study will not apply to an extended source or for a source whose angular size exceeds the resolution of the imager. This is because simple back-projection algorithms are not sufficient to resolve extended shapes.

Xu et al. (2004) estimated the source-to-detector distance by quantifying angular resolution as a function of the focal distance. Commonly, the calculation of angular resolution in Compton imaging requires knowledge of the source position, as angular resolution is the difference between the angle to the source measured by the detector and the known, true, angle to the source. In the method presented here, prior knowledge of the source location is not necessary. Additionally, the proposed method is a hybrid technique that uses simple back-projection to yield a quick source-to-detector estimate. Xu's method uses six iterations of the maximum likelihood expectation maximization (MLEM) algorithm per focal distance, as stated in the caption to Fig. 3 of their paper (Xu et al., 2004). The proposed method is of practical value to researchers because of its simplicity and speed.

2. Data collection and simulations using the PCI

The PCI consists of three silicon (Si) scattering planes. Each plane consists of a 16×20 array of 3 mm × 3 mm silicon pads, 0.28 mm thick, resulting in an active area of 48 mm × 60 mm for each plane. The silicon planes are mounted on the circuit boards of the readout electronics. A 6×7 array of 12 mm × 14 mm × 10 mm CsI(Tl) crystals, each with an attached silicon PIN diode, is also included. Readout electronics for the CsI crystals are mounted behind the array. The silicon planes are housed in a light-tight plastic bellows, and the CsI(Tl)/PIN diode array is housed in an aluminum casing. The silicon detector planes slide on nylon rods, making the spacing between the planes easily adjustable. The CsI(Tl)/PIN diode array is mounted directly behind the silicon detectors. Data were collected using a coincidence trigger between the scattering plane (one of the silicon planes) and the array of CsI(Tl)/PIN diodes (absorbing plane). This trigger allows for the collection of coincident interactions from the same photon in the scattering and absorbing plane, with a higher probability. In the reconstruction of events, it was assumed that the Compton scattering events took place in the scattering plane and absorption
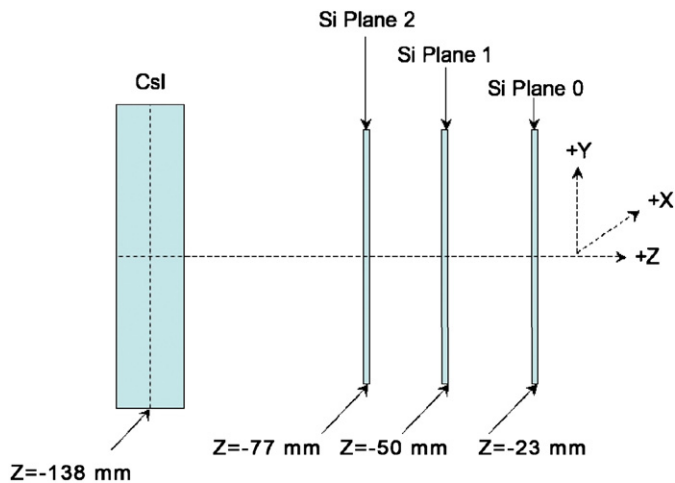
Fig. 2. Layout of the PCI. Only the active parts of the detector are shown. Three silicon planes (scattering detectors) are followed by a CsI array (absorbing detectors). The origin of the Z-axis is at the front of the box enclosing the silicon detectors, as shown on the right side of the figure. The PCI works well in the energy range of 300–1500 keV and at source-to-detector "Z" distances up to 200 mm.

Fig. 3. A sketch showing a series of lines originating at a random position on the detector plane (shown as a rectangle at left) and passing through a randomly selected position on the image plane. The image location is shown by a small box. The position in the detector plane is uniformly distributed along the length of the detector. The position on the image plane is randomly selected from a Gaussian distribution centered at the center of the image. If the image is reconstructed at any distance from the detector other than the correct distance, the reconstructed image will have a larger angular width than the true image.

took place in the absorbing plane, and that the incident gamma-ray energy was the sum of all recorded energy deposits. Fig. 2 shows the layout of the PCI and the coordinate system used. The centerline of the active areas of the silicon planes and the CsI(Tl) array are at $X = 0$ mm, $Y = 0$ mm. The positive Y direction goes up from the center of the plane, and the positive X direction goes into the paper. The Z position of each plane is shown in Fig. 2.

The PCI was modeled using the GEANT4 simulation toolkit (Agostinelli et al., 2003). Doppler broadening effects were modeled using the GLECS (GEANT low-energy Compton scattering) package (Kippen, 2004), an extension to GEANT4 that accurately models atomic binding effects for low-energy Compton and Rayleigh scattering. The model includes all major components of the PCI and any relevant shielding and housings that could cause scattering. In the simulations (as in the real detector), the active area of each silicon plane is divided into 320 pixels, each 3 mm × 3 mm, and the CsI consists of 42 separate sensors in a 6 × 7 array. The total is therefore 1002 discrete detector elements. The ^{137}Cs simulations consisted of 400 million simulated 662-keV gamma rays, thrown in a 30° cone toward the front of the detector. The output of the simulation is a list of detector elements that were hit and corresponding energies deposited in each detector element for a given event. During analysis, appropriate energy resolution was added to the data in order to more accurately model the prototype. The resolution of the silicon detectors was assumed to be 36 keV full-width half-maximum (FWHM) independent of energy. The resolution of the CsI detectors was assumed to be (for E in keV).

$$\text{FWHM} = \sqrt{(12.5\,\text{keV})E + \left(\frac{E}{13.7}\right)^2} \qquad (1)$$

Eq. (1) gives, for example, 103 keV FWHM (15.6%) for a 662 keV gamma ray. The assumed resolution for both silicon and CsI is based on, and in agreement with, experimental measurements. When used without the CsI detectors, the silicon resolution was somewhat better, but this time "jitter" in the CsI+silicon coincidence trigger resulted in the observed 36 keV silicon resolution.

A key assumption in this paper is that an image, when reconstructed at the correct distance from the detector, will have a smaller solid angle than an image reconstructed at any other distance from the detector. Fig. 3 illustrates the change in the size

of the reconstructed image versus distance from the detector. It is clear that both the size of the image and the angle it subtends (measured from the center of the detector plane) is minimized by reconstructing at the correct distance from the image. The variation in the solid angle with distance from the detector can be estimated through a simple calculation. First assume that each transverse (X and Y) position on the detector plane is equally likely to occur in an event—this is a reasonable approximation. All events are assumed to occur at the same value of Z—the small differences in the Z positions of the three silicon planes are ignored. Next, assume a Gaussian-shaped image at the position of the image. This Gaussian distribution will have an angular width described by σ_θ. The detector measures an angle—so this is the appropriate parameter to describe the size of the image. Given these assumptions, a ray connecting a point on the detector plane can be drawn. This ray is projected to the Z of the plane in which the image is reconstructed. Fig. 3 illustrates this process in one dimension. The mean square distance of the intersection of this ray from the center of the image on that plane is then calculated. This mean square distance of all rays from the image center is then divided by the distance of the image from the detector to give an estimate of the variation in solid angle (Ω) with the Z position of the plane on which it is reconstructed.

$$\Omega \approx \frac{A + R_0^2 \sigma_\theta^2}{R_0^2} - \frac{2AZ_0}{R_0^2}\frac{1}{Z_i} + \frac{AZ_0^2}{R_0^2}\frac{1}{Z_i^2} \qquad (2)$$

In this expression $A = (dx^2 + dy^2)/12$, dx and dy are the width (48 mm) and height (60 mm) of the silicon detector planes, R_0 is the true distance from the detector to the image, Z_0 is the true Z distance from the detector to the image, and Z_i is the distance at which the image was actually created. This expression reduces to the correct value $\Omega \approx \sigma_\theta^2$ as $R_0 \to \infty$ or when $Z_0 = Z_i$—meaning that the image size is defined by the detector's angular resolution when the source is far away or when the image is reconstructed at the correct value of Z. The expression has a minimum at Z_i—the true distance to the image. The second derivative of this function, when evaluated at its minimum is $2A/(R_0^2 Z_0^2)$—which approaches zero when the image is far from the detector (R_0 and/or Z_0 large). This shows that the minimum is well defined only when the source is close to the imager.

3. Data analysis

Raw experimental data was processed to select events for image reconstruction. The selection criteria for imaging events require energy deposited in exactly one silicon pixel and exactly one CsI crystal. The current method also attempts to determine the incident gamma-ray energy and places a window around events in the photo peak. An example of the chosen energy window is shown in Fig. 4. Fig. 4 was generated using measured data acquired using a ^{137}Cs source with an activity of approximately 370 kBq, located at (10, 38, 70) mm in the coordinate system used here (see Fig. 2 and the text describing it). The energy window placed on the events is indicated by the black highlighting and covers the photo peak. All the events that fall in this region were used in imaging. The CsI(Tl) energy resolution dominates the overall resolution in the PCI. Note the width of the energy window affects the number of events imaged.

Using these selected events, images were reconstructed at source-to-detector distances starting from 20 mm and going up to 200 mm in 10 mm steps. The solid angle of the image was calculated by summing the area of each pixel in the image (A_i) above a certain threshold value divided by 4π times the distance from the center of the pixel to the average scattering location of the data set squared. In (3) ΔZ represents the distance between the Compton interaction Z (averaged over all interactions) and the center of the imaging pixel. This expression assumes $A_i \ll R_i^2$, which is a good approximation in this case.

$$\Omega = \sum_i \frac{A_i}{4\pi R_i^2}, \quad R^2 = (\Delta X)^2 + (\Delta Y)^2 + (\Delta Z)^2 \tag{3}$$

The formula for calculation of solid angle (Ω) of the image for all pixels i above threshold is shown in (3). The threshold value is referred to as a peak threshold hereafter and is defined as the fraction of the maximum single-pixel amplitude in the image. For example, a peak threshold of 0.5 means that all of the pixels whose amplitude is above 0.5 times the maximum amplitude in the image will be included in the solid angle calculation. The solid angle subtended by each of the reconstructed images is then plotted against the corresponding source-to-detector distance. As shown in (2), the minimum solid angle subtended (in steradians) on this plot corresponds to the "real" source-to-detector distance (also see plots in Fig. 5).

Figs. 5A and B show the calculated solid angle of the reconstructed image as a function of imaging distance. The plots shown in Fig. 5 used a threshold value of 0.50. This value was
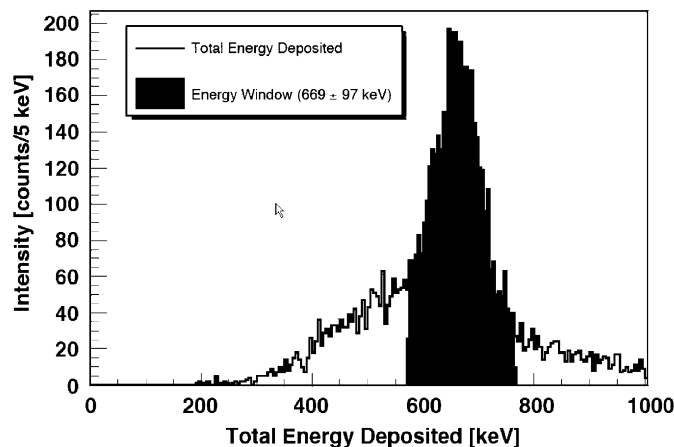
chosen for this example because it is the two-dimensional analog of the FWHM. As will be discussed later in this paper, the result is not very sensitive to this threshold parameter—any value from about 0.3 to 0.5 will give a similar answer. Smaller threshold values use more of the data and can reduce statistical uncertainties—but too low a value will start to include background. Conversely, larger values decrease the number of pixels used in the measurement while also reducing background. The two plots are for a source located at $X = 10$ mm, $Y = 38$ mm, and $Z = 70$ mm from the origin of the coordinate system. The top plot (Fig. 5A) shows simulated data and the bottom plot (Fig. 5B) shows the corresponding measured data. The minima of the plots shown in (Figs. 5A and B) were fit using (4) and the source-to-detector distance Z_{min} was estimated according to (5) with the computed fit parameters (P_1, P_2). The uncertainty in Z_{min} is shown in (5) where σ_1 and σ_2 are the uncertainties on P_1 and P_2, respectively. Eq. (4), which is based on (2), was used to fit the points around the minimum in order to improve the estimate of the source position. Here Z_{det} is the distance between the average Z location of the Si planes and the source. In the experiments the distance Z was the distance between the source and the front cover of the imager. Therefore, in (4) $Z_{det} = Z+dZ$, $dZ = 50$ mm for the set-up shown in Fig. 2.

$$\Omega = P_0 + P_1/Z_{det} + P_2/Z_{det}^2 \tag{4}$$

A P₀=0.013, P₁=-2.70, P₂=164.78

B P₀=0.087, P₁=-19.78, P₂=1184.21
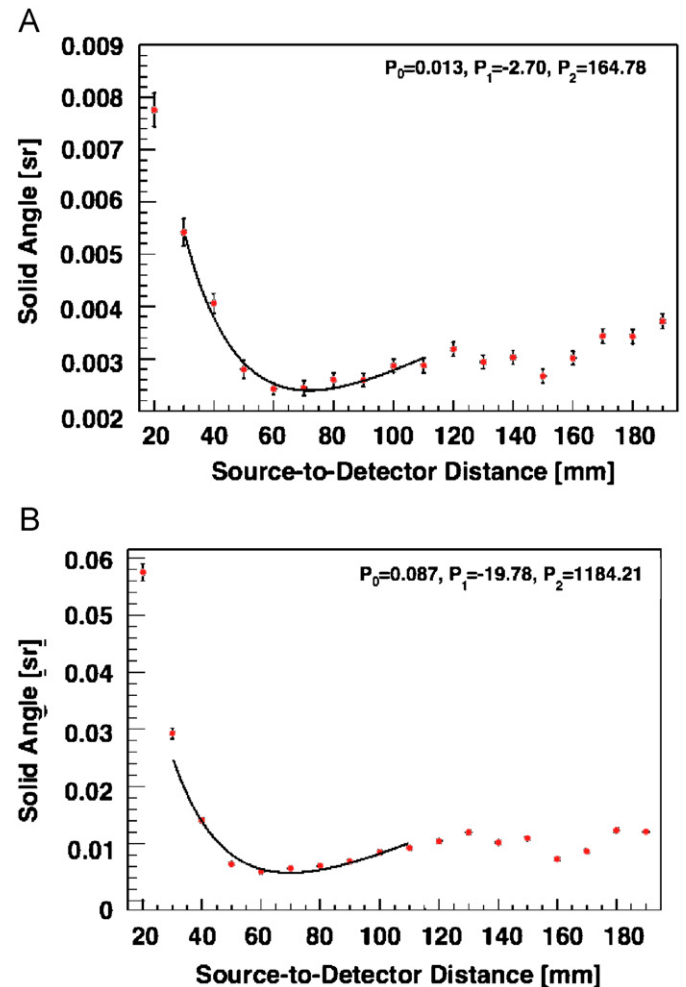
Fig. 5. Solid angle subtended by the reconstructed image vs. the source-to-detector distance. Plots are shown for both a simulated (A) and measured (B) off-axis ^{137}Cs point source. The fit to the minimum is shown with a dashed line. The source coordinates for both data sets are at ($X = 10$ mm, $Y = 38$ mm, and $Z = 70$ mm). The fits use (4). The threshold for this figure was 0.50.

Fig. 4. Total energy deposited in the PCI. Energy window is highlighted in black. The width of the energy window is 194 keV (669±97). These results are from experimental measurements.

$$Z_{min} = (-2P_2/P_1) - dZ \qquad (5)$$

$$\sigma_{min} = Z_{min}\sqrt{(\sigma_1/P_1)^2 + (\sigma_2/P_2)^2} \qquad (6)$$

In (4) Ω is the corresponding solid angle in steradians. The expected size of the image is minimized when the correct image plane is used—as is illustrated in one dimension by Fig. 2.

Using the fits from Fig. 5 without varying further parameters (threshold = 0.50), Z_{min} was estimated to be 69.7 ± 6.2 mm for measured data (Fig. 5B) and 72.1 ± 17.2 mm for the corresponding simulated data (Fig. 5A). The real source distance is 70 ± 3 mm. It should be noted that the accuracy of the estimated source-to-detector distance depends on several factors: the statistical uncertainty in the numbers of reconstructed events, peak threshold, pixel size, and finite position and energy resolution of the PCI. The effects of detector position and energy resolution on the ability to determine X, Y, and Z are described in the literature and will not be reiterated here (An et al., 2007).

Out of the remaining parameters, the largest effect comes from limited statistical precision of the image. There are two types of statistical effects. First, statistical uncertainty in the number of reconstructed events is dependent on the width of the energy window set around the photo peak (an example is shown in Fig. 4), and second, calculation of the solid angle depends on the peak threshold, which limits the number of pixels used in the calculation. A plot of the deviation from true Z (ΔZ) as a function of energy window width is shown in Fig. 6. From this plot, it can be seen that as the width of the energy window decreases, the deviation from the true Z becomes slightly larger. The statistical uncertainties are shown as a gray band in Fig. 6—the statistical uncertainties on adjacent points are correlated. Once the energy window is wide enough ($\sim$10 keV), more and more events from the continuum with incomplete energy collection in the PCI are included in image reconstruction, which adds to the uncertainty by degrading the angular resolution. In general, it is necessary to include all the events in the photo peak while minimizing the number of continuum events. However, in this example, most events are in the photo peak, so a larger energy window does not significantly damage the Z position resolution. Currently, the window width is based on the measured FWHM resolution of the PCI as a function of incident photon energy.
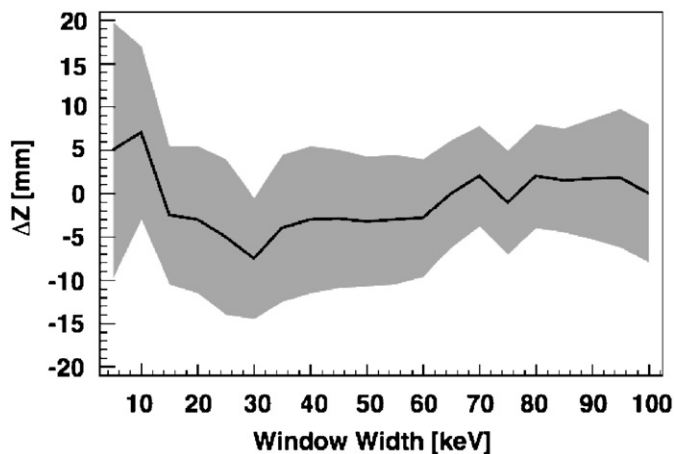
Once the energy window was determined, the pixel area, A_i in (1), was chosen ($A_i = 13.7$ mm^2) to be smaller than the known position resolution of the PCI. Care was taken to assure that this area was not so small that the time required for reconstruction became unnecessarily large. The next parameter that affects the determination of the source-to-detector distance is the peak threshold. A plot of the difference (ΔZ) between the actual Z position of the source and the calculated Z position (Z_{min}) vs. peak threshold for measured data is shown in Fig. 7. For this particular data set, Z_{min} estimates are relatively stable between threshold values of 0.3 and 0.5. In fact, for all of the cases tested, the value of Z_{min} did not vary significantly when the threshold value was changed from 0.3 to 0.5. Therefore, in each case, the average value of Z_{min} for this range of threshold values was taken rather than arbitrarily choosing any particular value. Using this average gave better results (meaning the calculated Z value is closer to the actual Z) than any particular value of the threshold parameter—so this average is used as the best estimate of the actual Z. Because the statistical uncertainties on the points being averaged are correlated, we estimated the statistical uncertainty on the average to be the average of the error bars. The average of the Z_{min} estimates for the PCI dataset is shown in Fig. 7. The applied fit produced an estimated Z_{min} value of 70.6 ± 5.4 mm. The actual Z in this case was at 70 ± 3 mm.

Multiple data sets were also simulated for various source locations using the technique described here. We also used this method on sources with different gamma-ray energies (^{137}Cs, ^{54}Mn, and ^{60}Co). We found the values for Z to have a similar accuracy to the dataset described in greater detail here. Results of Z determinations for ^{137}Cs, ^{54}Mn, and ^{60}Co sources are tabulated in Table 1.

All results were obtained using a Dell Precision 670 workstation with a 3.8 GHz processor running Linux. Determining the Z distance of a point source for the example shown in Fig. 7 requires about 1 min of runtime, depending on the size of the pixels in the image. This time could be reduced considerably (with a some loss in accuracy) by choosing a particular value of the threshold rather than doing the calculation at $\sim$30 different values (as was done here) and taking the average of the results.

Fig. 6. Plot of the difference (ΔZ) between the actual Z position of the source and the calculated Z position vs. energy-window width in keV. This data set is a measured data set using ^{137}Cs source at ($X = 10$ mm, $Y = 38$ mm, and $Z = 70$ mm). The shaded region shows the statistical uncertainty and the line shows the calculated value.
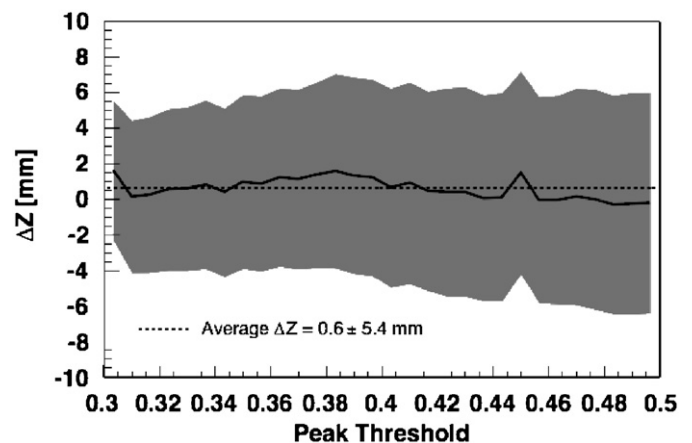
Fig. 7. The difference between the calculated source Z position and the actual source Z position vs. peak threshold. Average Z_{min} was estimated to be 70.6 ± 5.4 mm with a fit between 0.3 and 0.5 peak threshold values. The actual Z value was 70.0 ± 3.0 mm and is shown by the dotted line. This plot was generated using measured data set with ^{137}Cs source that was located at ($X = 10$ mm, $Y = 38$ mm, and $Z = 70$ mm). The shaded region shows the statistical uncertainties, the solid line shows the calculated value, and the dotted line shows the average of all the calculated values.

Table 1
Energy and average Z_{min} for three other measured data sets

Source	Incident energy (keV)	Z_{min} (mm)	Actual Z (mm)	Actual X, Y (mm)
^{60}Co	1173, 1333	75.9 ± 3.1	80 ± 3	0, −30
^{54}Mn	834	61.8 ± 6.5	70 ± 3	10, 38
^{137}Cs	662	103.2 ± 16.2	100 ± 3	0, −60

4. Conclusions

An algorithm that uses the solid angle subtended by the reconstructed image as a function of the source-to-detector distance is used to estimate the imaging distance in the Z dimension. The method was validated using both measured and simulated data. Results from data and simulations were comparable. The method described here is able to determine the Z position of the single point source when the distance to the source is not too much larger than the transverse (X and Y) dimensions of the detectors. This algorithm does not require prior knowledge of the X and Y location of the source, nor does it require calculating them at any time in the procedure. In this case, the method accurately estimates the Z distances up to about 200 mm. The silicon detectors are 48×60 mm in X and Y, and the CsI array is 87×89 mm. The accuracy in the Z determination is approximately ± 10 mm. We simulated a case where we increased the lateral size of the PCI detectors to 1 m $\times$ 1 m. We assumed the same pixilation and energy resolution for individual elements as before, although such an instrument would not be cost effective. For a photon source of 662 keV located at a $Z = 2$ m, we were able to estimate the source-to-detector distance of 2.08 ± 0.13 m. At 3 m, the estimated source distance was 3.09 ± 0.30 m. One option for improving the resolution in source-to-detector distance would be to use two imagers, separated by a significant distance to give the system views from multiple angles—thereby improving the distance resolution.

References

Agostinelli, S., et al., 2003. Geant 4—a simulation toolkit. Nucl. Instrum. Methods A 506 (3), 250–303.

An, S.H., et al., 2007. Effect of detector parameters on the image quality of Compton camera for Tc-99m. Nucl. Instrum. Methods Phys. Res. Sect. A 1, 123.

Haskins, P.S., et al., 1996. Point source resolution performance of a germanium Compton camera. IEEE Trans. Nucl. Sci. 43 (3), 1832–1836.

Hoover, A.S., et al., 2006. Gamma-ray imaging with a Si/CsI(Tl) Compton detector. Appl. Radiat. Isot. 64 (12), 1648–1654.

Kippen, R.M., 2004. The GEANT low energy Compton scattering (GLECS) package for use in simulating advanced Compton telescopes. New Astron. Rev. 48 (1–4), 221–225.

Kurfess, J.D., et al., 2004. An advanced Compton telescope based on thick, position-sensitive solid-state detectors. New Astron. Rev. 48, 293–298.

Mihailescu, L., et al., 2007. SPEIR: a Ge Compton camera. Nucl. Instrum. Methods Phys. Res. Sect. A 570 (1), 89–100.

Morhac, M., et al., 1997. Efficient one- and two-dimensional gold deconvolution and its application to gamma-ray spectra decomposition. Nucl. Instrum. Methods Phys. Res. Sect. A 401, 384–408.

Nguyen, M.K., et al., 2001. Apparent image formation by Compton scattered photons in gamma-ray imaging. IEEE Signal Process. Lett. 8, 248–251.

Niedermayr, T., et al., 2005. Gamma-ray imaging with a coaxial HPGe detector. Nucl. Instrum. Methods Phys. Res. 553 (3), 501–511.

Sullivan, J.P., et al., 2003. Detector tests for a prototype Compton imager. In: IEEE Nuclear Science Symposium Conference Record. Medical Imaging Conference (2), pp. 1384–1388.

Vetter, K., et al., 2007. High-sensitivity Compton imaging with position-sensitive Si and Ge detectors. Nucl. Instrum. Methods Phys. Res. Sect. A 579 (1), 363–366.

Xu, D., et al., 2004. 4π Compton imaging with single 3D position sensitive CdZnTe detector. In: Proceedings of SPIE—the International Society for Optical Engineering, Hard X-ray and Gamma-Ray Detector Physics VI 5540, pp. 144–155.